Gold- and Silver-Coated Barium Titanate Nanocomposites as Probes for Two-Photon Multimodal Microspectroscopy

Fani Madzharova, Álvaro Nodar, Vesna Živanović, Michael R. S. Huang, Christoph T. Koch, Rubén Esteban, Javier Aizpurua, and Janina Kneipp

Improved multiphoton-excited imaging and microspectroscopy require nanoprobes that can give different nonlinear optical signals. Here, composite nanostructures with a barium titanate core and a plasmonic moiety at their surface are synthesized and characterized. It is found that the core provides a high second-order nonlinear susceptibility for sensitive second harmonic generation (SHG) imaging in living cells. As a second function in the two-photon regime, the plasmonic part yields high local fields for resonant and nonresonant surface enhanced hyper Raman scattering (SEHRS). SEHRS complements the one-photon surface enhanced Raman scattering (SERS) spectra that are also enhanced by the plasmonic shells. Barium titanate silver core–shell (Ag@BaTiO$_3$) composites are specifically suited for SEHRS and SHG excited at 1064 nm, while gold at barium titanate (Au@BaTiO$_3$) nanoparticles can be useful in a combination of SHG and SERS at lower wavelengths, here at 785 nm and 850 nm. The theoretical models show that the optical properties of the BaTiO$_3$ dielectric core depend on probing frequency, shape, size, and plasmonic properties of the surrounding gold nanoparticles so that they can be optimized for a particular type of experiment. These versatile, tunable probes give new opportunities for combined multiphoton probing of morphological structure and chemical properties of biosystems.

1. Introduction

Optical spectroscopy opens up exciting new possibilities for visualization and monitoring of bioorganic molecules and structures, in particular for the investigation of basic chemical and physical processes in biosystems. In addition to widely used linear optical effects, including fluorescence[1] and Raman scattering (RS),[2] nonlinear processes have become very attractive in laser microspectroscopy and imaging. They include two-photon-excited fluorescence,[3] second harmonic generation (SHG),[4] stimulated Raman scattering[5] and coherent anti-Stokes Raman scattering[6] microscopies, and imaging based on spontaneous hyper Raman scattering (HRS).[7] Nonlinear processes are attractive in microscopy and spectroscopy since they can be excited with light in the near-infrared, which offers several advantages. The latter include deep tissue penetration capability, reduced photodamage due to the lower photon energy, and spatially more confined probed volume, which can result in an improved lateral resolution.[8] Nevertheless, when multiphoton-excited processes are complemented with their one-photon-excited counterparts, this can yield unprecedented structural information from a sample. As an example, the spontaneous two-photon-excited Raman process, termed HRS, is governed by different selection rules than the (conventional) spontaneous one-photon-excited RS. Both HRS and RS can be enhanced in the local fields of plasmonic nanostructures, resulting in surface enhanced hyper Raman scattering (SEHRS)[9] and surface enhanced Raman scattering (SERS) spectra, respectively. While imaging based on vibrational spectra gives detailed molecular structure, other nonlinear optical signals, such as SHG, are less specific but lead to information about the microscopic morphology of a sample. SHG is a two-photon process, where a

F. Madzharova, Dr. V. Živanović, Prof. J. Kneipp
Department of Chemistry
Humboldt-Universität zu Berlin
Brook-Taylor-Str. 2 12489, Berlin, Germany
E-mail: janina.kneipp@chemie.hu-berlin.de

The ORCID identification number(s) for the author(s) of this article can be found under https://doi.org/10.1002/adfm.201904289.

Á. Nodar, Prof. J. Aizpurua
Centro de Física de Materiales CFM-MPC (CSIC-UPV/EHU)
Paseo Manuel de Lardizabal 5 20018, San Sebastián-Donostia, Spain
Dr. M. R. S. Huang, Prof. C. T. Koch
Department of Physics and IRIS Adlershof
Humboldt-Universität zu Berlin
Newtonstr. 15 12489, Berlin, Germany
Dr. R. Esteban, Prof. J. Aizpurua
Donostia International Physics Center (DIPC)
Paseo Manuel de Lardizabal 4 20018, San Sebastián-Donostia, Spain
Dr. R. Esteban
IKERBASQUE
Basque Foundation for Science
Maria Diaz de Haro 3 48013, Bilbao, Spain

non-centrosymmetric macromolecule or nanostructure yields an effective combination of two photons into a single photon of twice the frequency of the incident beam.

Several generations of optical nanoprobes and labels, strongly varying in chemical composition and size range, have been developed to match the specific requirements of multiphoton-excited methods regarding functionality. Among others, they include customized organic dyes[10] and quantum dots[11] for one- and two-photon-excited fluorescence, perovskite-type nanocrystals as harmonic probes for SHG,[12] and gold and silver nanoparticles that can be used as plasmonic probes for SEHRS imaging of cells and tissues.[13] The combination of linear and nonlinear microspectroscopy, such as of SHG with two-photon fluorescence and conventional RS,[4c,14] or of SERS with SEHRS,[7c,13a] creates a strong demand for nanoprobes with multiple optical modalities, in order to provide complementary and more reliable information by joining the strengths of different spectroscopic methods.[15] Extending the capabilities of nanoprobes that deliver chemical information through a vibrational signature with the requirements of fast nonlinear imaging would allow truly multimodal optical imaging based on both chemical structural information with morphology at the microscopic level, and thus could be very beneficial for microspectroscopic studies of biological objects.

Here, we report about the synthesis and optical characterization of gold- and silver-coated barium titanate composite nanoparticles and demonstrate that they can be utilized as multifunctional optical nanoprobes for SHG, SERS, and SEHRS, thereby providing complementary information for imaging as well as for vibrational spectroscopy. We chose barium titanate as the core material because of its nonlinear optical properties and well established use as harmonic probe in SHG biomicroscopy.[12a,16] As will be discussed, surrounding the barium titanate nanocrystals with a shell of gold and silver nanoparticles allows to take advantage of the strongly enhanced Raman and hyper Raman process in the near fields of these plasmonic structures, and thus enables sensitive vibrational probing of the local surface environment by means of SERS and SEHRS, which can provide complementary chemical and structural information of target samples due to the different selection rules for the one-photon and two-photon-excited spontaneous Raman process.[9] In particular, we show that our composite nanoparticles can enhance Raman and hyper Raman scattering, while simultaneously acting as suitable SHG nanoprobes, which is demonstrated by applying them for combined SHG and vibrational imaging in macrophage cells. In order to understand how the optical properties of dielectric barium titanate particles are altered by the presence of the plasmonic shell, we compare the experimental SHG data with theoretical simulations.

2. Results and Discussion

2.1. Preparation and Characterization of the Composite Nanostructures

To prepare SHG and SERS/SEHRS active composite nanostructures, commercially available polycrystalline barium titanate (BaTiO$_3$) nanoparticles in the tetragonal crystal structure were used as starting material. The diameter of the particles was 256 ± 84 nm, as determined from transmission electron microscopy (see Figure S1 in the Supporting Information). **Scheme 1** shows a simplified representation of the synthetic route for obtaining the composite nanostructures, a more detailed reaction scheme can be found in Section S1 in the Supporting Information. In the first step, barium titanate particles were pretreated with hydrogen peroxide to increase the amount of surface hydroxyl groups (see Figure S2 in the Supporting Information for infrared spectra)[17] so that the subsequent silanization with (3-aminopropyl)triethoxysilane (APTES) or (3-mercaptopropyl)trimethoxysilane (MPTMS) would be promoted.

It should be noted that the reaction with hydrogen peroxide, if carried out at high temperature compared to room temperature, visibly modifies the surface layer of the barium titanate nanoparticles (see the inset in Figure S3 in the Supporting Information) possibly caused by an excessive loss of barium ions that leads to the degradation of the particle surface and
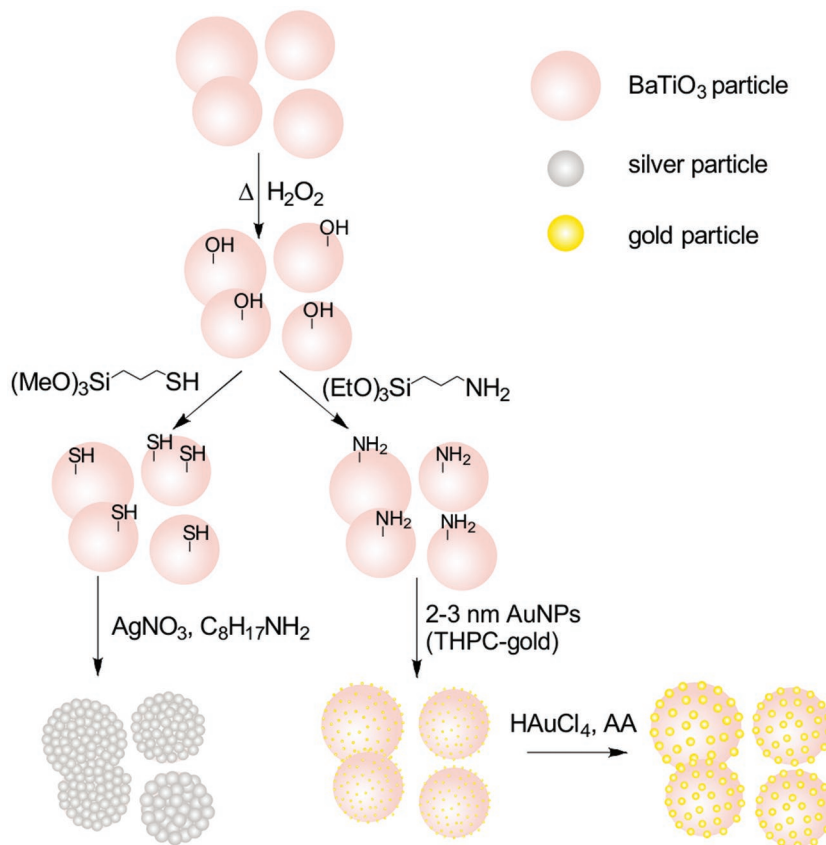
Scheme 1. Schematic representation of Au@BaTiO$_3$ and Ag@BaTiO$_3$ nanocomposite preparation. Also see the Experimental Section and Section S1 in the Supporting Information.

its structure.[18] Figure S3 (Supporting Information) shows that, while this modified surface layer is favorable for growing a gold shell in the next synthesis steps, it is not affecting the intensity of the SHG signals from the particles that will be discussed in detail in the next section.

For the synthesis of gold-coated barium titanate nanoparticles, termed Au@BaTiO$_3$ here, a seed-mediated growth approach was applied. Briefly, small gold seeds (≈2–3 nm) were attached to the surface of APTES-functionalized BaTiO$_3$ nanoparticles (Figure S4, Supporting Information) following previously suggested approaches,[18a,19] and then another protocol was adapted[20] to reduce gold chloride with ascorbic acid in their presence and in the presence of hexadecyltrimethylammonium bromide (CTAB).[19a,20] **Figure 1**A and Figure S5 (Supporting Information) show transmission electron microscopy (TEM) images and scanning transmission electron microscopy (STEM) energy-dispersive X-ray spectroscopy (EDS) maps of the barium titanate particles with ≈9 nm sized gold nanoparticles on their surface. Further gold deposition cycles resulted in an increased size of the gold nanoparticles and their detachment from the barium titanate surface. This is indicated by the presence of unbound gold nanoparticles in the supernatant, as shown by the band at 530 nm in the UV–vis spectrum of the solution obtained after precipitation of the composite structures (Figure S6, Supporting Information). On the other hand, if barium titanate particles with a hydrogen peroxide modified surface layer (Figure S3, Supporting Information) were used, the size of the gold nanoparticles could be increased to ≈17 nm without significant detachment

(Figure 1B; Figure S7, Supporting Information). The TEM images show that the gold particles reside partially inside the modified barium titanate surface layer that probably hinders their separation from the BaTiO$_3$. In both types of Au@BaTiO$_3$ nanostructures shown in Figure 1A,B, mainly single gold nanoparticles are densely distributed on the barium titanate surface, and no continuous gold shell is formed. The X-ray diffraction (XRD) pattern of the Au@BaTiO$_3$ particles shown in Figure S8A (Supporting Information) confirms the presence of barium titanate and gold, in accord with the EDS data (Figure 1A; Figure S7H, Supporting Information).

Figure 1C presents UV–vis absorbance spectra of the Au@BaTiO$_3$ nanocomposites. The pristine barium titanate particles have a broad absorbance with a maximum around 480 nm, which is also present in the spectra of the composite structures. The spectra of the gold coated nanoparticles, 9 nm Au@BaTiO$_3$ and 17 nm Au@BaTiO$_3$, show additional bands at 550 and 578 nm, respectively. The emergence of new resonant peaks in other related configurations has been explained by the excitation of the plasmonic modes of the metallic particles shifted by the dielectric environment,[21a,b,c] and it could also be due to an interaction and/or aggregate formation of neighboring gold nanoparticles on the barium titanate surface. As will be discussed in more detail below, an alternative picture, treating the gold nanoparticles as a homogeneous layer characterized by effective optical properties which modify the resonances of the bare barium titanate particles can also be considered.[21d,e]

We also prepared barium titanate-silver core–shell nanocomposites, termed Ag@BaTiO$_3$ here, by adapting a seedless
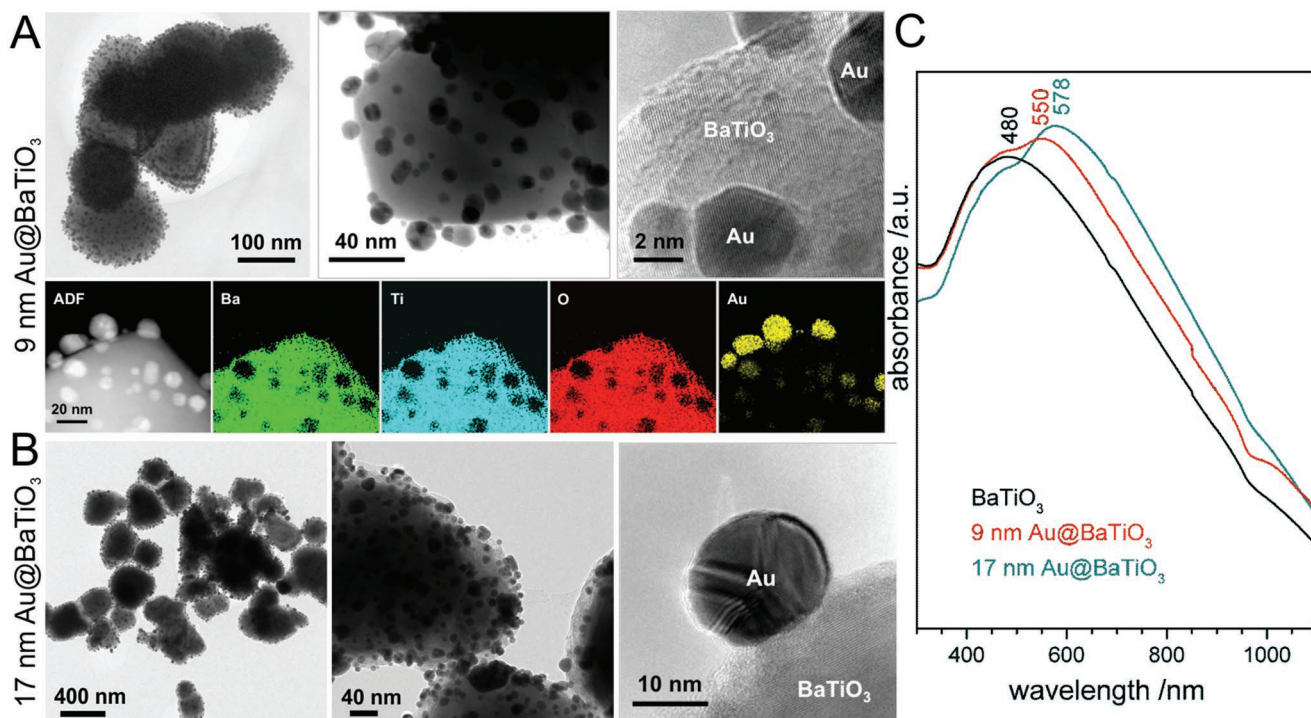

Figure 1. A) Transmission electron micrographs and STEM-EDS mapping of barium titanate particles with 9 ± 2 nm gold particles (9 nm Au@BaTiO$_3$). More TEM micrographs are provided in Figure S5 (Supporting Information). B) TEM images of barium titanate particles with 17 ± 6 nm gold particles on their surface (17 nm Au@BaTiO$_3$). More TEM micrographs and STEM-EDS mapping data are provided in Figure S7 (Supporting Information). C) UV–vis spectra of BaTiO$_3$ particles (black line), 9 nm Au@BaTiO$_3$ (red line), and 17 nm Au@BaTiO$_3$ (green line).

**ADVANCED
SCIENCE NEWS**
www.advancedsciencenews.com

**ADVANCED
FUNCTIONAL
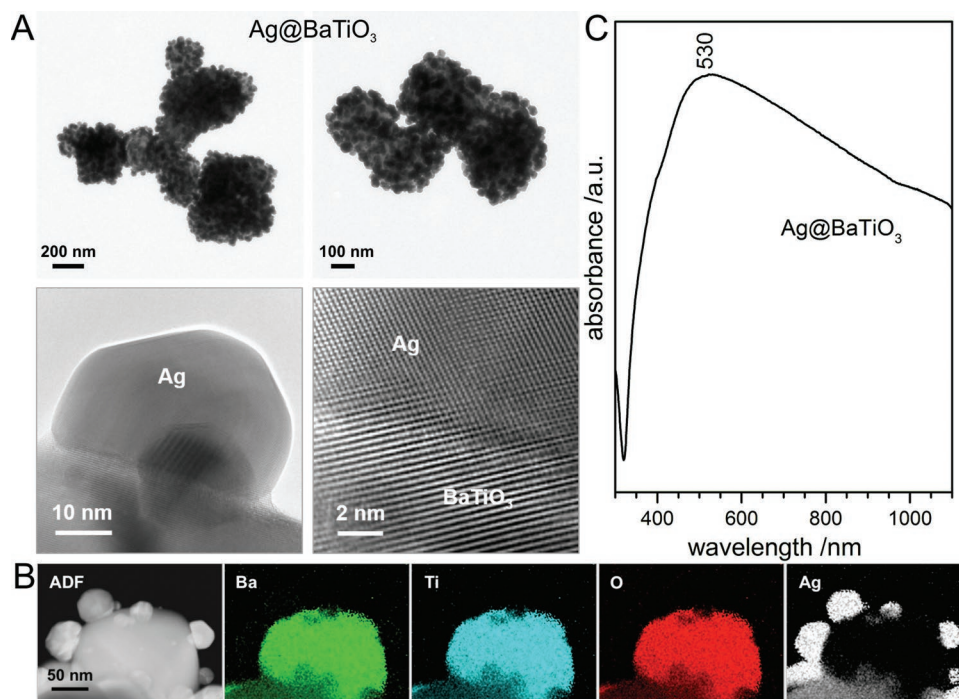MATERIALS**
www.afm-journal.de

Figure 2. A) Transmission electron micrographs and B) STEM-EDS mapping of barium titanate particles with 40 ± 9 nm silver nanoparticles on their surface (Ag@BaTiO$_3$). For more TEM images, see Figure S9 in the Supporting Information. C) UV–vis spectrum of Ag@BaTiO$_3$.

one-step synthetic route originally proposed for silica-silver core–shell structures.[22] Silver nitrate was reduced with a weak reducing agent, octylamine, in the presence of MPTMS-functionalized barium titanate particles and polyvinylpyrrolidone (PVP) in ethylene glycol (Scheme 1). This approach yielded barium titanate particles with almost continuous silver shells that consist of aggregated silver nanoparticles with an average diameter of ≈40 nm (**Figure 2**A; Figure S9, Supporting Information). EDS mapping (Figure 2B) and XRD of Ag@BaTiO$_3$ (Figure S8B, Supporting Information) show that the composite particles consist of barium titanate and silver. The UV–vis absorbance spectrum of the Ag@BaTiO$_3$ nanocomposites (Figure 2C) exhibits a very broad band from the visible to the near-IR with a maximum at 530 nm, which we attribute to the formation of silver nanoparticle aggregates on the barium titanate surface.[23]

2.2. Dual Two-Photon Probing by SHG and SEHRS in Combination with SERS

SHG of the plasmonic barium titanate nanocomposite systems was investigated using pulsed laser excitation at 850 nm and 1064 nm. We obtained strong SHG signals from aqueous solutions of all composite nanoparticles in backscattering collection geometry at both wavelengths. An example is presented in **Figure 3**A, and shows the quadratic dependence of the SHG signal on excitation intensity of Au@BaTiO$_3$ excited at 850 nm. This confirms the two-photon parametric process of SHG.

For SHG imaging experiments, J774 macrophage cells were used as a biological model system. In order to increase their biocompatibility and uptake by the cells, the nanoprobes were exposed to lipids following a protocol reported in ref. [24].

The SERS spectra at 785 nm excitation generated by the plasmonic moieties of the Au@BaTiO$_3$ nanoprobes (Figure S10A, Supporting Information, black spectrum), show characteristic bands at 761, 963, and 1449 cm^{-1} that are assigned to the stretching vibrations of the trimethylammonium headgroup and CH$_2$ twisting and wagging vibrations of CTAB,[25a] confirming stabilization of the nanoprobes by the capping agent. After incubation with lipid vesicles, these bands disappear (Figure S10A, Supporting Information, red spectrum), indicating displacement of CTAB from the nanoparticle surface. The absence of SERS signals from the CTAB as well as from the reporter molecules when 9 nm Au@BaTiO$_3$ nanocomposites were used, different to the 17 nm Au@BaTiO$_3$, indicates that the enhancement of the Raman scattering depends on the plasmonic properties of the gold nanoparticles in such a situation, and thus it is influenced by the gold particle size and by their interaction on the surface of the BaTiO$_3$. The 785 nm excited spectra of the Ag@BaTiO$_3$ composites (Figure S10B, Supporting Information, black line) exhibit weak bands at 1586, 1411, and 1077 cm^{-1} that can be assigned to the reducing agent octylamine,[25b,c] and a more pronounced band at 892 cm^{-1}, which can be caused by ring modes of PVP.[25d]

The macrophage cells were incubated with culture medium containing lipid coated 9 nm and 17 nm Au@BaTiO$_3$ and Ag@BaTiO$_3$ composite nanoprobes for 3 h. SHG maps of the cells at 850 nm excitation are shown in Figure 3B–K. According to previous discussions, we expect that the endogenous SHG from the biological cells is predominantly forward-propagated and much weaker than the signals from a nonlinear nanocrystal.[12a] Thus, we conclude that the SHG maps show the spatial distribution of the nanoprobes inside the macrophage cells. Comparing the absolute SHG signals from the nanoprobes
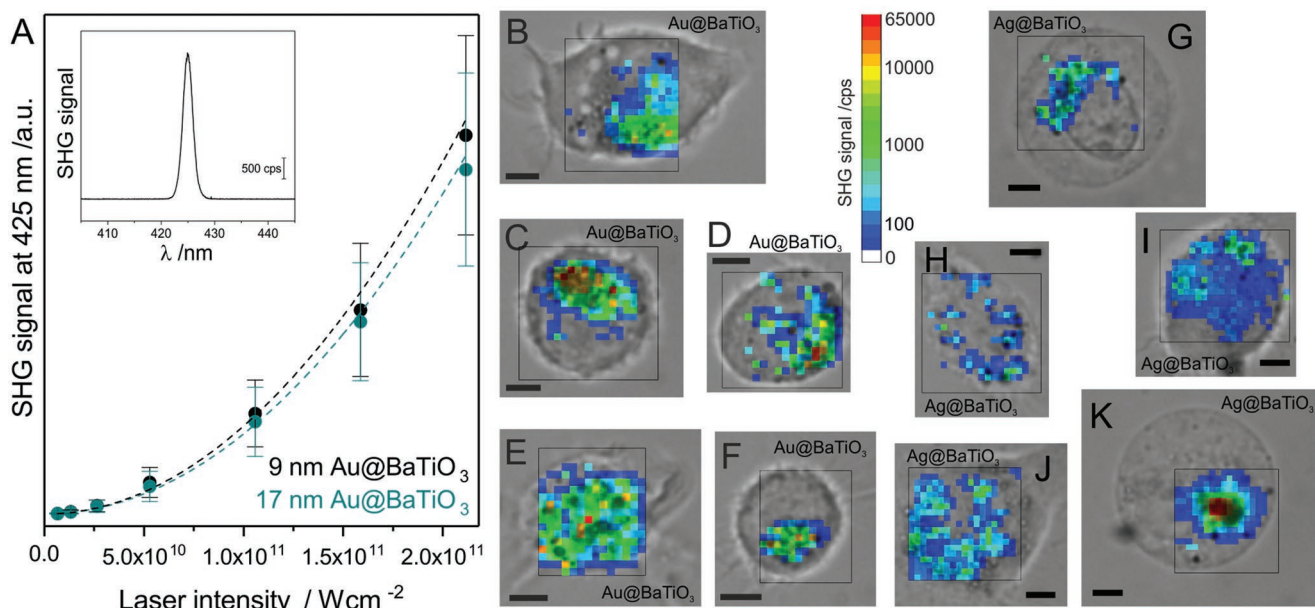
Figure 3. A) SHG signal from 9 nm Au@BaTiO$_3$ (black) and 17 nm Au@BaTiO$_3$ (green) excited at 850 nm as a function of the peak laser intensity. The values are the mean of 30 measurements with 1 s acquisition time; the dotted lines are the fitted quadratic curves ($ax^2 + b$) to the data points. The inset shows an SHG spectrum of 17 nm Au@BaTiO$_3$ at 5×10^{10} W cm^{-2}. B–K) Bright-field images of J774 macrophage cells containing lipid-coated 9 and 17 nm Au@BaTiO$_3$ B–F) and Ag@BaTiO$_3$ G–K) nanocomposites, overlaid with SHG maps. The color bar applies to all images (B)–(K). Excitation: 850 nm; acquisition time: 1 s; peak laser intensity: 1×10^{11} W cm^{-2} (5 mW average power); step size: 1 µm; scale bars: 5 µm.

in the cells with those measured in solution, the former can be significantly higher at some positions in the cells, in agreement with the known formation of aggregate structures in endosomes inside the cellular ultrastructure.[26]

In addition to the possibility of obtaining such morphofunctional information from the cells by SHG imaging, the plasmonic moieties allow molecular and structural characterization of the local surface environment of the metal-barium titanate nanoprobes by means of SERS. As shown above, SERS can probe the presence of the CTAB capping agent and monitor its displacement. SERS spectra of small molecules such as crystal violet (Figure S11, Supporting Information) that were added to aqueous suspensions of 17 nm Au@BaTiO$_3$ and Ag@BaTiO$_3$ nanoparticles show that molecules interact with the surface of the nanocomposites, and their spectra can be obtained using NIR wavelengths for excitation, not in resonance with electronic transitions in the dye molecules.

The collection of such nonresonant SERS spectra is one of the main prerequisites for biological applications of the new optical probes, and for the collection of spectra from the cellular environment.[13a] As an example of such a potential application as reporters in live cells, 17 nm Au@BaTiO$_3$ and Ag@BaTiO$_3$ nanocomposites were modified with *para*-mercaptobenzoic acid (*p*MBA), and nonresonant SERS mapping of J774 macrophage cells incubated with the nanoparticles was conducted. **Figure 4**A–D shows chemical maps of the cells based on the SERS intensity of the *p*MBA ring stretching vibration at 1070 cm^{-1}. The molecules remained on the surface of the nanocomposites after 3 h of cellular uptake, confirmed by the stable SERS signals of *p*MBA obtained from the

cells. These results demonstrate that the metal-barium titanate composite nanostructures can be the basis of SERS tags that highlight biological structures in one-photon-excited vibrational imaging experiments[13a,27] in addition to the two-photon probing.

Probing of intrinsic cellular structures without reporter molecules using lipid coated Au@BaTiO$_3$ particles in macrophage cells is presented in Figure 4E. The SERS spectra show lipid bands due to the lipid coating of the nanoprobes or of cellular membranes,[28] and also bands that are characteristic of other molecules in the cells. For example, while the band at 714 cm^{-1}, present in most of the spectra, is very characteristic for the C–N stretching of the choline group in lipids, the bands at 827 and 853 cm^{-1} can be assigned to aromatic amino acids with high Raman cross sections that are abundant in proteins.[29] The SERS spectra of the intrinsic cellular molecules (Figure 4E) provide a perspective on the chemical environment of the nanoprobes, and thereby complement the morphological information obtained by SHG (Figure 3B–K).

As it is demonstrated in **Figure 5**, the plasmonic moiety of the Ag@BaTiO$_3$ nanoparticles permits the collection of SEHRS spectra. Using an excitation wavelength of 1064 nm, resonant SEHRS spectra of the dye molecule crystal violet (CV) were obtained with Ag@BaTiO$_3$ (Figure 5, bottom trace). They resemble SEHRS of CV previously reported in work using gold and silver nanoparticles.[7c,30] The nonresonant SEHRS spectrum of *p*MBA (Figure 5, top trace), a very sensitive indicator of pH inside and outside cells,[31] exhibits characteristic bands corresponding to the ring stretching and symmetric ring breathing modes of the molecule at 1578 and 1072 cm^{-1},
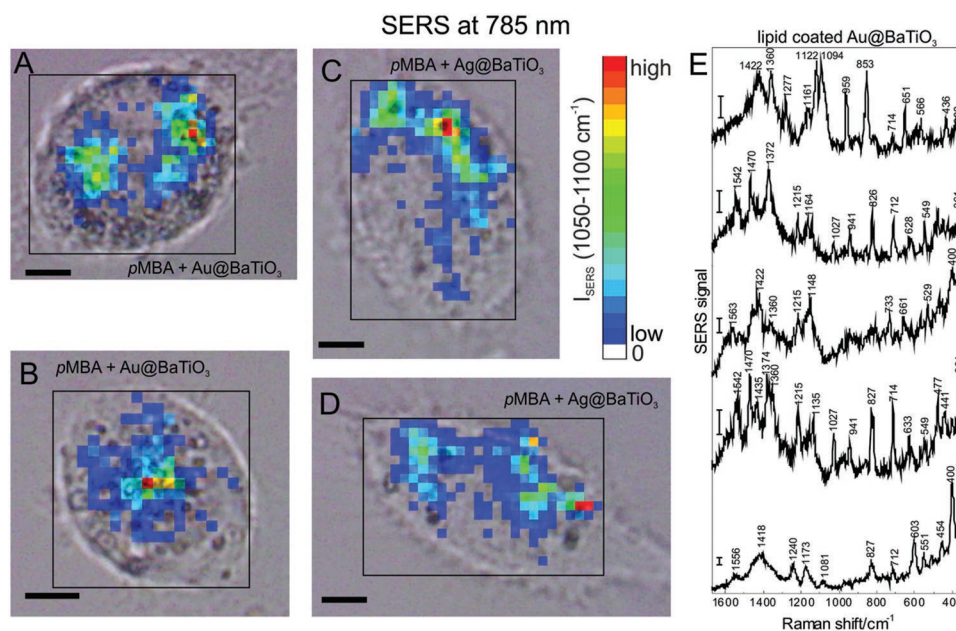
**ADVANCED
SCIENCE NEWS**

www.advancedsciencenews.com

**ADVANCED
FUNCTIONAL
MATERIALS**

www.afm-journal.de

Figure 4. A–D) Bright-field images of J774 macrophage cells containing *p*MBA-labeled 17 nm Au@BaTiO₃ A,B) and Ag@BaTiO₃ C,D) nanocomposites, overlaid with Raman maps based on the integrated SERS signal of the reporter. Excitation: 785 nm; acquisition time: 1 s; laser intensity: 8×10^5 W cm^{-2} (4 mW average power); step size: 1 µm; scale bars: 5 µm. E) SERS spectra at 785 nm from J774 cell after 3 h uptake of lipid coated 17 nm Au@BaTiO₃. Scale bars: 20 counts s^{-1}.

respectively.[32] The presence of the band corresponding to the C–COO⁻ stretching at 1364 cm^{-1} enables pH mapping in cells with *p*MBA-labeled Ag@BaTiO₃.[31] Here, SEHRS microspectra are excited at a wavelength that enables imaging of the plasmonic barium titanate nanoprobes by SHG as well, and hence two different two-photon imaging modalities can be used at the same time.

2.3. Influence of the Plasmonic Moiety on the SHG Properties

In order to understand how the SHG efficiency of the barium titanate nanocrystals is altered when they are surrounded by the plasmonic nanostructures, we performed simulations of the far- and near-field properties of different model systems which mimic the nanostructures in our experiments. First, we use Mie theory[33] to calculate the extinction cross sections of a BaTiO₃ sphere of 300 nm diameter in water (**Figure 6**A, black dashed line). We also check that we are able to converge the results using the finite-difference time domain (FDTD) method (brown line, superimposed with the black one), which is useful for later comparisons. The extinction cross section of the BaTiO₃ sphere has three peaks in the considered spectral range at 447, 545, and 714 nm. The decomposition of the total Mie extinction cross section (Figure 6A, black dashed line) into separate multipole contributions (Figure 6A, red, green, and blue lines) shows that, the peaks at 447, 545, and 714 nm correspond to the maxima of the magnetic octopole, magnetic quadrupole and magnetic dipole modes, respectively. Similar resonances have been found in previous studies of nanostructures with positive (dielectric) permittivity.[34] The theoretical extinction shows several narrow and well-defined peaks, in

contrast to the broad maxima in the experimental measurements (Figure 1C). This effect can be trivially assigned to an inhomogeneous broadening in the experiment due to the size and configuration dispersion within the colloids.

The extinction of the Au@BaTiO₃ composite particle is calculated using FDTD simulations. In these calculations, the BaTiO₃ sphere considered above is covered by 600 uniformly distributed gold spheres of 17 nm diameter. The spectrum is shown in Figure 6B by the brown line (see Figure S12 in the Supporting Information for the study of the convergence). We also plot in the same panel the results obtained when we consider a homogeneous metallic shell on the BaTiO₃ dielectric core to effectively mimic the response of the metallic cluster on the particle (Figure 6B, black dashed line). The effective permittivity of this coating is given by Maxwell–Garnett theory,[21e] and the shell system is then solved with Mie theory.[33,35] Both approaches give very similar results, consistent with previous work,[21d,e] so that it is possible to use the contributions of each term in the Mie expansion to identify the multipole modes in the composite particle. Figure 6B indicates that in the gold coated barium titanate particle, the magnetic octopole, quadrupole and dipole resonances are redshifted to 454, 625, and 789 nm, respectively (Figure 6B). The fourth peak in the extinction cross section of the Au@BaTiO₃ composite at 526 nm has contributions from many modes, mainly the magnetic and electric quadrupoles (Figure 6B). If the size of the core particle is decreased, all resonances in both the coated and pristine barium titanate spheres are blueshifted (see Figure S13 in the Supporting Information).

Figure 6C,D shows the distributions of the electric and magnetic near-field at the extinction cross section peaks of the two types of structures. Although we have typically associated these
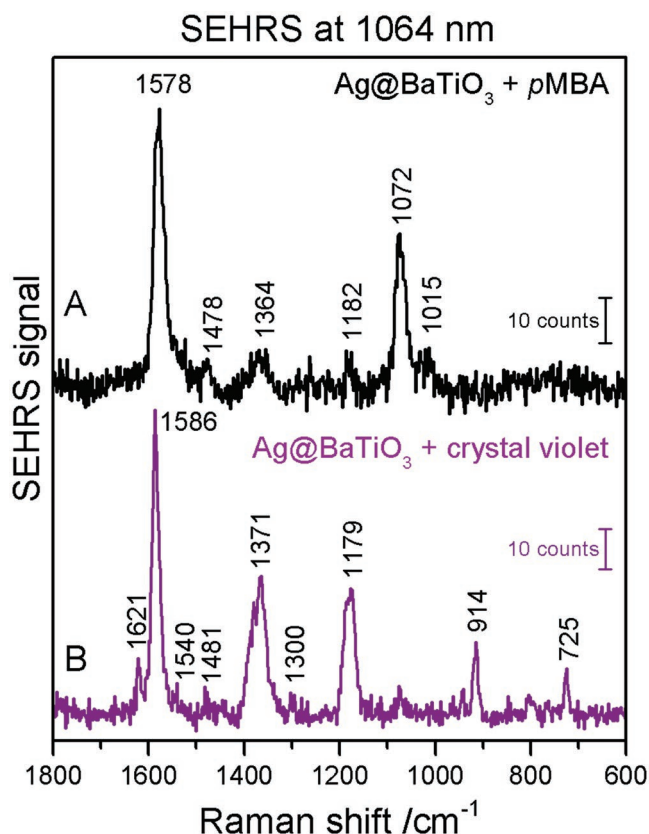
Figure 5. SEHRS spectra of A) *para*-mercaptobenzoic acid (*p*MBA) and B) crystal violet (CV) situated in the local fields of Ag@BaTiO$_3$. Excitation: 1064 nm; acquisition time: 300 s A) and 60 s B); peak laser intensity: 2×10^{10} W cm^{-2} A) and 6×10^9 W cm^{-2} B). CV concentration was 1×10^{-6} M; Ag@BaTiO$_3$ were incubated with 10^{-4} M *p*MBA for several hours and the excess *p*MBA was removed by centrifugation and washing cycles.

peaks to a specific magnetic multipolar resonance, the near fields present mixed features due to the overlapping contribution of other off-resonant electric and magnetic multipoles.[34b] For the dielectric BaTiO$_3$ sphere, the electromagnetic field is concentrated mainly inside the material, and the field at the surface of the particle is relatively low with values of $|E_{loc}/E_0|$ of ≈2 (Figure 6C, left panels), where E_0 is the amplitude of the incident electric field and E_{loc} the corresponding value of the total local fields (sum of the incident and induced fields). In contrast, the densely distributed gold nanoparticles on the Au@BaTiO$_3$ composite surface provide high electric field enhancement in their proximity (Figure 6D, left panels). The resulting SERS enhancement, which scales approximately with $|E_{loc}/E_0|^4$, reaches values up to 10^4, especially for the longer wavelengths of 625 and 789 nm. This indicates that, although enhancement of optical scattering processes in high refractive index dielectric nanostructures is possible,[34a,d] the observed SERS and SEHRS in our experiments here (Figures 4 and 5, respectively) should mainly result from the enhanced local fields generated by the plasmonic moieties.

On the other hand, this plasmonic enhancement does not necessarily dominate the SHG. The fields inside the entire BaTiO$_3$ core must be taken into account, and not just those in the proximity of the metallic nanoparticles. According to previous experimental work, the second harmonic generation from barium titanate nanocrystals is frequency dependent.[12a,34c] Particularly, the SHG is enhanced at the intrinsic optical resonances of the particle.[34c,36] In our systems, the simulated extinction cross sections of both the pristine and gold coated BaTiO$_3$ spheres (Figure 6A,B) showed that the multipole resonances of the two particles are located at different positions. Thus, we would expect different frequency-dependent profiles of the intensity of SHG signals from bare and gold coated barium titanate particles. Here, we have measured SHG from pristine BaTiO$_3$ nanocrystals and Au@BaTiO$_3$ nanocomposites at 1064 and 850 nm excitation. The results are compared in **Figure 7**. While for excitation at 1064 nm the SHG signal from Au@BaTiO$_3$ composites is ≈4 times lower (in the whole intensity range) relative to the signal from pristine BaTiO$_3$ particles (Figure 7A, compare red and black symbols), at 850 nm the SHG intensity of the composites is only ≈2 times lower than that from the bare BaTiO$_3$ particles (Figure 7B, compare red and black symbols). Similar results were obtained for Ag@BaTiO$_3$ composites (Figure S14, Supporting Information), with a decrease of the SHG intensities for Ag@BaTiO$_3$ relative to the pristine BaTiO$_3$ particles (Figure S14A,B, Supporting Information). Comparing the effect of different excitation wavelengths on the signals from Au@BaTiO$_3$ (Figure 7) and Ag@BaTiO$_3$ (Figure S14, Supporting Information), the composites with silver yielded higher SHG signals at 1064 nm than at 850 nm, while the composites with gold showed higher SHG signals at 850 nm than at 1064 nm. Due to the fact that our lasers operate in different power ranges, we refrain from a comparison of absolute intensities at both excitation wavelengths. Nevertheless, the different ratios for SHG intensity from pristine and metal coated BaTiO$_3$ particles at the two different excitation wavelengths clearly indicate the frequency dependence of the SHG signals from plasmonic barium titanate nanocomposites.

In order to understand the different ratios of the SHG, we use the information of the near fields simulated in our model systems to estimate the SHG enhancement for excitation angular frequency ω. Calculating the exact SHG for polycrystalline particles is very complex, and we just follow a simplified approach that decomposes the total enhancement into two different contributions. The first is associated with the generation of a polarization oscillating at 2ω inside the spherical dielectric core, due to the nonlinear susceptibility of BaTiO$_3$. This is a second-order process, leading to an enhancement that scales with the fourth power of the local electric field amplitude $E_{loc}(\omega)$ (second power of the local intensity) at the excitation frequency ω. The second contribution (which multiplies the first one), is due to the change of the emission rate of the excited 2ω polarization. Due to reciprocity,[37] the increase of the field emitted from each infinitesimal region of the BaTiO$_3$ sphere can be approximated as the enhancement of the local electric field amplitude $E_{loc}(2\omega)$ at the same region for planewave illumination at 2ω (or, equivalently, the intensity of the emitted signal scales with the square of the local fields). We then estimate the SHG intensity from the composite particle relative to the corresponding signal from the bare sphere as
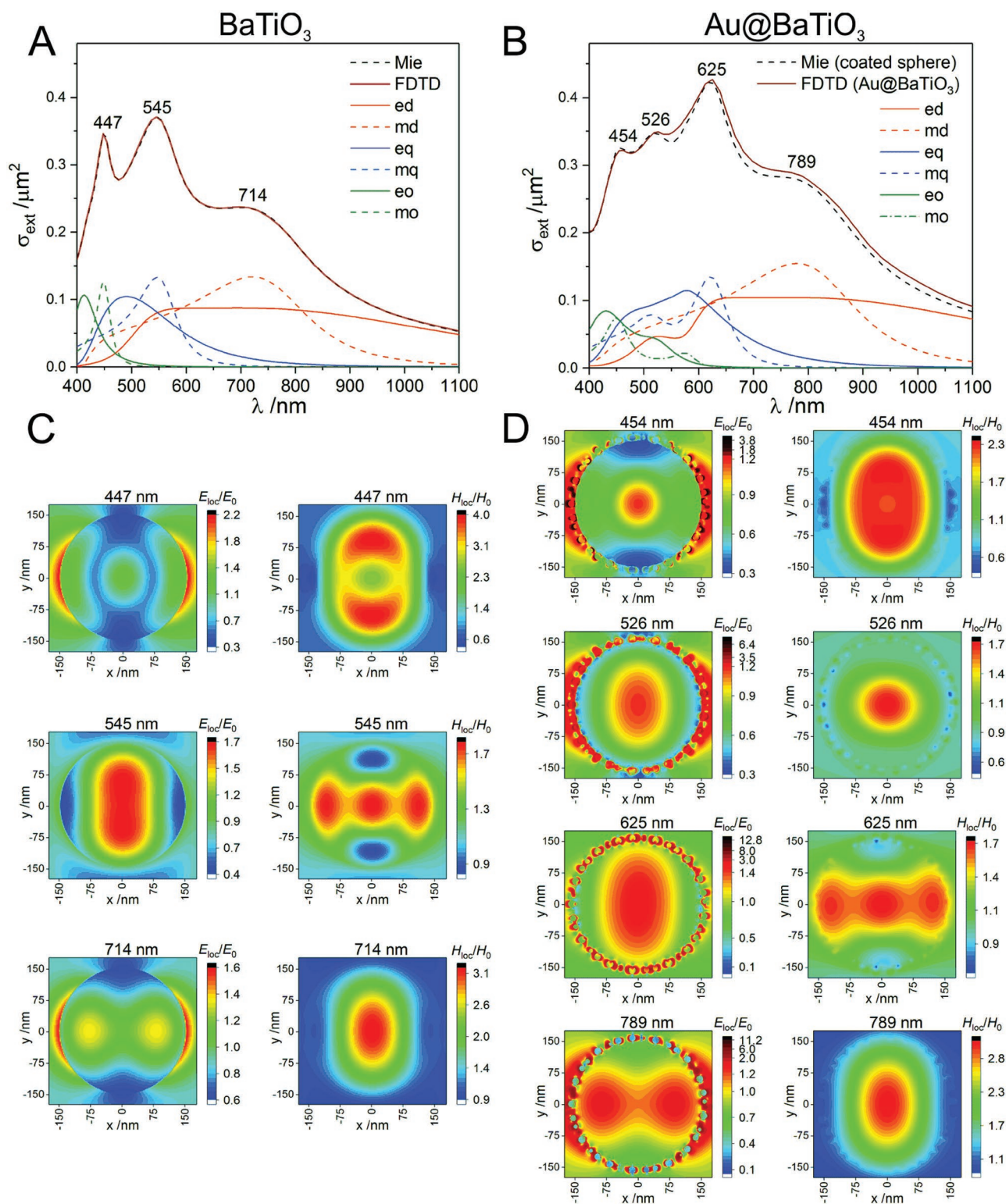
Figure 6. Extinction cross sections of A) barium titanate sphere (300 nm diameter) and B) barium titanate sphere (300 nm diameter) with 600 gold spheres (17 nm diameter) on its surface calculated with FDTD and Mie theory (using the effective medium approximation). Legend for the Mie expansion—ed and md: electric and magnetic dipole (red); eq and mq: electric and magnetic quadrupole (blue); eo and mo: electric and magnetic octopole (green). C,D) Maps for the modulus of the total electric and magnetic fields normalized to the incoming electric and magnetic fields, respectively (E_{loc}/E_0 and H_{loc}/H_0), in the xy-plane for C) the 300 nm barium titanate sphere from (A) and D) the composite 300 nm barium titanate sphere with gold nanospheres on its surface from (B). The fields are evaluated at the frequencies corresponding to the total extinction cross sections peaks. The field distributions were calculated from FDTD, where a plane wave propagating in the $-z$ and polarized in the x direction was used.
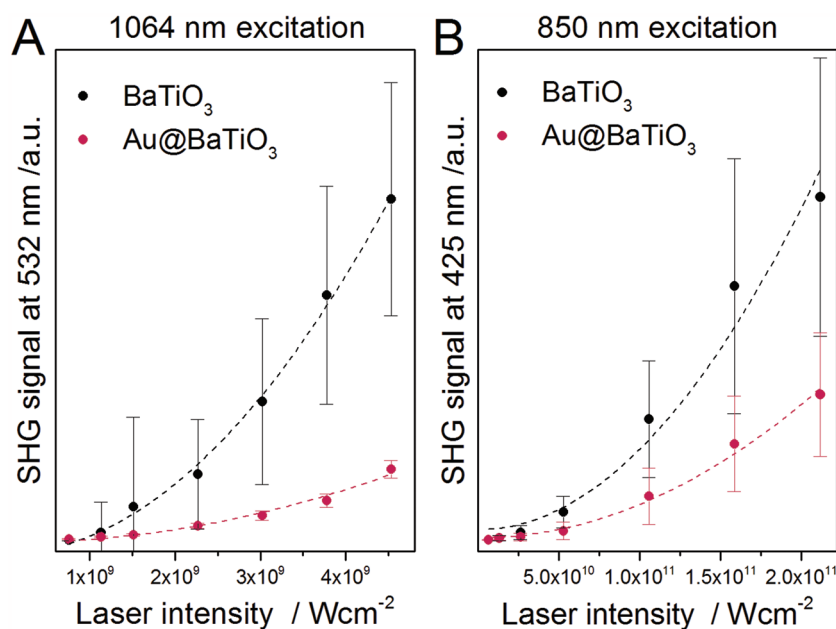
Figure 7. SHG signal from aqueous solutions of BaTiO$_3$ nanoparticles (black) and 17 nm Au@BaTiO$_3$ nanocomposites (red) with similar concentration excited at A) 1064 nm and B) 850 nm as a function of the peak laser intensity. The values are the mean of 30 measurements; the dashed lines are the fitted quadratic curves ($ax^2 + b$) to the data points. Integration time: 20 s A) and 1 s B).

$$\frac{I_{SHG}(Au@BaTiO_3)}{I_{SHG}(BaTiO_3)} \propto \frac{\left(\int E_{loc}^2(\omega,\mathbf{r},Au@BaTiO_3)dV\right)^2}{\left(\int E_{loc}^2(\omega,\mathbf{r},BaTiO_3)dV\right)^2} \frac{\int E_{loc}^2(2\omega,\mathbf{r},Au@BaTiO_3)dV}{\int E_{loc}^2(2\omega,\mathbf{r},BaTiO_3)dV} \quad (1)$$

where the integral takes into account the contributions from the entire BaTiO$_3$ sphere, with the distribution of fields obtained from the FDTD simulations. We do not consider the emission from the gold nanoparticles, because gold is a centrosymmetric material with no bulk SHG, and furthermore we assume the surface contributions to be negligible compared to the signal from BaTiO$_3$. Equation (1) integrates over the real-valued amplitudes of the fields, and thus assumes a loss of spatial coherence, which we justify by the presence of many crystalline domains with different crystallographic orientations. A loss of SHG coherence due to polycrystallinity has already been discussed and observed in related systems.[38] Equation (1) may underestimate the role of the small regions of strong, highly-confined fields (plasmonic hot spots) induced inside the BaTiO$_3$ by the small gold nanoparticles, but we believe that their influence in our experiment is small. In the Supporting Information, we further discuss Equation (1) and compare it with other coherent and incoherent expressions, the latter derived for monocrystalline particles. The equations including loss of coherence give similar trends, but, as expected, larger differences are found when comparing the coherent and incoherent expressions for the emission. This suggests that the loss of coherence can have a significant impact on the actual SHG, which points out towards the need of characterizing the

polycrystallinity of the particles for precise theoretical analysis of nonlinear emission in complex nanoenvironments.

Figure 8 shows the integral of the square of the electric field amplitude $\int E_{loc}^2 dV$ inside the core sphere in the considered wavelength range for a 300 nm BaTiO$_3$ particle and a 300 nm BaTiO$_3$ particle with small gold nanospheres on their surface, as a model to describe the Au@BaTiO$_3$ system. Three clear peaks appear in both spectra due to the magnetic dipole, quadrupole and octopole (compare with the corresponding extinction cross section in Figure 6A,B). The moderate spectral shift with respect to the extinction results can be attributed to the effect of the strong losses.[39] While the electric field at the magnetic octopole resonance in the gold-coated BaTiO$_3$ is clearly reduced relative to that of the bare BaTiO$_3$ sphere, the field intensities at the magnetic quadrupole and dipole resonances are comparable in both structures. The latter though are redshifted in the Au@BaTiO$_3$ composite. Because of these changes in the distribution of the local fields, we estimate that, according to Equation (1), the SHG intensity from the composite particle should be ≈90% for the excitation at 850 nm and ≈60% at 1064 nm relative to the intensity from the bare barium titanate nanocrystal.

In Table S1 in the Supporting Information, we have summarized the expected relative SHG signal strengths for core barium titanate particles of different size and shape. Both, size and shape have strong influence on the positions of the multipole resonances (Figure S13 and Table S1, Supporting Information), and on the electric fields inside the particle (see Figure S15 in the Supporting Information). For all model systems that we have investigated here, the relative SHG intensities at 850 nm are higher than at 1064 nm, which is in qualitative agreement with the experimental data (Figure 7). For example, while the SHG signal of a 250 nm BaTiO$_3$ cuboid surrounded by gold nanospheres is ≈80% at 850 nm and ≈55% at 1064 nm relative to the ones of a cuboid without gold particles (compare red and black lines in Figure S15C in the Supporting Information), the relative values for a 255 nm sphere are ≈130% and ≈80% (compare red and black lines in Figure S15B in the Supporting Information), respectively. The latter also indicates that an enhancement of SHG due to the gold coating is possible and could be achieved by careful tuning of the nanocomposite structure or by using a different excitation wavelength, e.g., further in the IR, in order to match the multipole resonances of the composite particles. The strong dependence of the SHG on the size of the barium titanate core particle is further illustrated in Figure S16 (Supporting Information), where the relative SHG values for many different core sphere sizes are calculated analytically using Mie theory and the effective medium approximation to model the gold shell (same model as the one used to calculate the extinction cross section in Figure 6B, black dashed line).
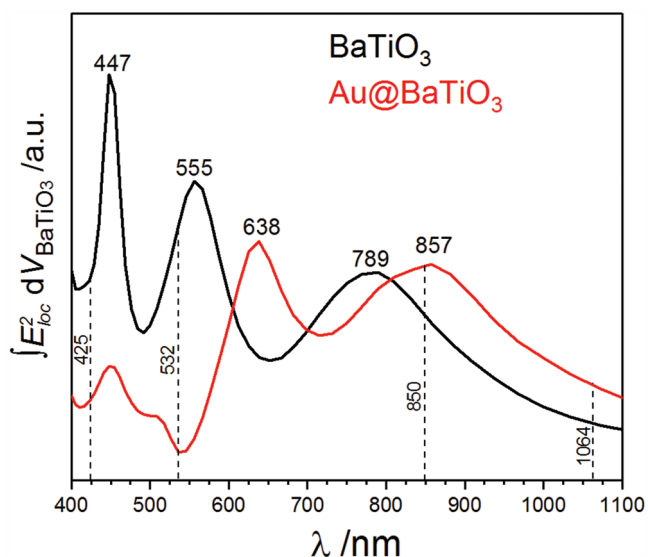
ADVANCED
SCIENCE NEWS
www.advancedsciencenews.com

ADVANCED
FUNCTIONAL
MATERIALS
www.afm-journal.de

Figure 8. Integral over the square of the electric field amplitude inside the volume of the barium titanate structure for a bare 300 nm barium titanate sphere (black) and a 300 nm barium titanate sphere with 600 gold nanospheres on its surface (red) as a function of the wavelength and calculated with FDTD.

Considering the actual situation in the experiments, in particular the very broad size distribution, the nonspherical shape of the barium titanate particles (Figure S1, Supporting Information), as well as the influence of surrounding nanoparticles, including, e.g., the reabsorption of the light emitted from one particle by others in the solution, our estimate of the relative SHG efficiency is in reasonable agreement with the experimental SHG data. We conclude that the observed SHG intensity from the composite nanostructures in our experiments (Figure 7) is affected by shifts of the particles' electromagnetic modes, and the corresponding changes in the electric fields inside the nonlinear nanocrystal when a plasmonic shell is present. On the other hand, the plasmonic nanoparticles at the outside provide enhancement of the electric fields in their proximity, which enable electromagnetic enhancement in SEHRS and SERS, as evidenced by SEHRS (Figure 5) and SERS spectra.

3. Conclusion

We have synthesized composite nanostructures consisting of a barium titanate core, a material with high second-order nonlinear susceptibility, and a plasmonic moiety of gold or silver nanoparticles at the surface of the core that can act as versatile optical nanoprobes for a combination of two different two-photon-excited microscopies, together with one-photon-excited SERS. In the nonlinear regime, the composite nanostructures function as harmonic probes for SHG, as well as plasmonic substrate that enhances resonant and nonresonant hyper Raman scattering. By delivering SEHRS spectra, the composite nanoprobes provide vibrational information that is complementary to the one-photon-excited SERS spectra, also obtained here using nonresonant excitation. As demonstrated by the observation of their aggregation in live cells, the strong

SHG signals at short integration times and low excitation intensities of the probes can be used to image physiological functions and nanomaterials processing in biological systems.

Both, experimental data and theoretical simulations indicate that the strength of the SHG signals from the nanocomposites is wavelength dependent. Due to changes of the optical near field properties induced by the presence of the plasmonic nanostructures, SHG can decrease moderately relative to that obtained from plain barium titanate particles. As a second aspect, the gold and silver particles on the barium titanate surface also enhance the local fields in their surroundings, which opens new opportunities for probing of the local environment by means of Raman and hyper Raman scattering. We have shown this by detecting molecules and their changing interaction on the surface of the composite nanostructures with SERS and SEHRS. The data show that depending on the plasmonic coating, the optical properties of barium titanate nanocrystals can be tuned and optimized for a particular type of experiment. The Ag@BaTiO$_3$ composites were specifically suitable for SEHRS and SHG excited at 1064 nm, as well as SERS at 785 nm, while the Au@BaTiO$_3$ nanoparticles can be useful in experiments that combine SERS and SHG at lower wavelengths, in our case at 785 nm and 850 nm, respectively. In conclusion, the results demonstrate that plasmonic barium titanate nanocomposites are versatile, tunable probes for multimodal multiphoton microspectroscopy and may open up new avenues for studying the morphological structure and chemical properties of biosystems.

4. Experimental Section

Materials: All chemicals were purchased from the following sources and used without further purification: gold(III) chloride trihydrate (HAuCl$_4$·3H$_2$O, 99.9%), silver nitrate (99.9999%), (3-aminopropyl)triethoxysilane (APTES, 99%), (3-mercaptopropyl)trimethoxysilane (MPTMS, 95%), tetrakis(hydroxymethyl) phosphonium chloride solution (THPC, 80% in water), *n*-octylamine (99%), hexadecyltrimethylammonium bromide (CTAB, 98%), polyvinylpyrrolidone (PVP, molecular weight 40 000), 4-mercaptobenzoic acid (*p*MBA, 99%), ethylene glycol (EG, 99%), L-ascorbic acid (AA, 98%), L-α-phosphatidylcholine (99%), and phosphate buffered saline (PBS) from Sigma Aldrich; ammonium hydroxide solution (25%), and sodium hydroxide (97%) from Fluka; crystal violet (CV) from J. T. Baker; hydrogen peroxide solution (30%) from Roth; barium titanate particles (BaTiO$_3$, tetragonal, 99.9%) from US Research Nanomaterials, Inc. All solutions were prepared using Milli-Q water (USF Elga Purelab Plus purification system). For cell cultures, Dulbecco's modified Eagle's medium (DMEM), fetal calf serum (FCS), and ZellShield were purchased from Biochrom AG, Berlin, Germany.

Ag@BaTiO$_3$ Nanoparticle Synthesis: For the preparation of silver barium titanate composite nanoparticles, a protocol for surface functionalization of barium titanate with hydroxyl groups[17] and a protocol for growing silver shells on silica cores[22] were adapted and optimized. Barium titanate nanoparticles (30 mg) were dissolved in hydrogen peroxide (30%, 10 mL) and sonicated for 1 h at room temperature. The particles were centrifuged at 7500 rpm for 15 min and washed with water several times, and then redispersed in 50 mL ethanol. Ammonium hydroxide (25%, 80 μL) and MPTMS (200 μL) were added subsequently to the BaTiO$_3$ particles and the mixture was stirred over night at room temperature. The particles were centrifuged for 15 min at 7500 rpm and washed with ethanol several times to remove excess reagents, then redispersed in 10 mL ethanol.

2 mL of the MPTMS-functionalized $BaTiO_3$ particles was centrifuged, redispersed in 2 mL ethylene glycol, placed in a round bottom flask, and stirred at room temperature. Silver nitrate solution in ethylene glycol (3 mL, 1 g L^{-1}), PVP solution in ethylene glycol (2 mL, 0.2 g L^{-1}), and n-octylamine (5 µL) were added subsequently and the reaction mixture was stirred for 2 h. The particle solution turns from white to yellow, to gray pinkish, and finally to dark brown. To remove unbound silver nanoparticles, the Ag@$BaTiO_3$ particles were centrifuged for 10 min at 2000 rpm and washed with ethanol many times until the supernatant was transparent. Finally, the particles were dispersed in 2 mL ethanol and stored at room temperature. For further experiments, the particles were typically centrifuged, redispersed in water and diluted as stated below.

Au@$BaTiO_3$ Nanoparticle Synthesis: For the preparation of gold barium titanate composite nanoparticles, protocols for surface functionalization of barium titanate and a seed-mediated growth approach for the gold shell formation were adapted.[16a,18a,19,20] Barium titanate particles (180 mg) were dissolved in hydrogen peroxide (30%, 30 mL) and sonicated for 30 min at room temperature. Then, the particles in hydrogen peroxide were heated in an oil bath under reflux at 110 °C for 4 h. The heating step was omitted when preparing Au@$BaTiO_3$ with smaller gold particles as shell. The particles were centrifuged at 7500 rpm for 30 min and washed with water several times, and then redispersed in 300 mL ethanol. Ammonium hydroxide (25%, 480 µL) and APTES (2.5 mL) were added subsequently to the hydroxylated $BaTiO_3$ particles in ethanol and the mixture was stirred for 6 h at 75 °C under reflux. The particles were centrifuged for 20 min at 7500 rpm and washed with ethanol at least three times to remove excess reagents, then redispersed in 60 mL ethanol. Gold nanoparticles with size of 2–3 nm (THPC-gold) were prepared as reported previously and aged for at least one week.[40] APTES-functionalized barium titanate nanoparticles in ethanol (5 mL) were mixed with THPC-gold (5 mL), shaken with vortex mixer for 2–3 min, and left still overnight. Successful generation of THPC-gold functionalized $BaTiO_3$ nanoparticles was verified by TEM (Figure S4, Supporting Information). The THPC-gold functionalized $BaTiO_3$ particles were centrifuged for 10 min at 6500 rpm and washed with water three times, then redispersed in 5 mL water, and used as the seeds in the next step. CTAB solution (2 mL, 0.2 M) was mixed with HCl (100 µL, 1 M) and $HAuCl_4$ (1 mL, 0.75 × 10^{-3} M) in a 15 mL centrifuge tube under vortex shaking. Then, ascorbic acid (150 µL, 0.01 M) was added and the solution was shaken until it turned transparent. Finally, 2 mL of the seeds were injected in the reaction mixture; the tube was shaken for 10 s and left still in a water bath at 30 °C for 30 min. The particles were centrifuged for 10 min at 2000 rpm and washed with water several times until no unbound gold nanoparticles were present in the supernatant, and finally redispersed in 2 mL water, containing CTAB (2 µL, 0.2 M) to increase stability. This procedure yields ≈9 nm gold nanoparticles distributed on the surface of the barium titanate cores. In order to increase the size of the gold nanoparticles to ≈17 nm, one more growing cycle was performed by using the product as seeds. CTAB solution (1.5 mL, 0.2 M) was mixed with HCl (75 µL, 1 M), $HAuCl_4$ (0.75 µL, 0.67 × 10^{-3} M), ascorbic acid (100 µL, 0.01 M), and 1.5 mL of the product from the previous step in the same conditions as described above. After several centrifugation and washing cycles, the particles were redispersed in 1.5 mL water, containing CTAB (2 µL, 0.2 M) to increase stability, and stored at room temperature. For further experiments, the particles were typically centrifuged, redispersed in Milli-Q water and diluted as stated below.

Characterization Methods: UV–vis spectra were recorded with a UV–vis–NIR double-beam spectrophotometer (V-670, Jasco) in the wavelength range between 300 and 1200 nm in quartz cuvettes of 10 mm path length. The transmission electron microscopy (TEM) characterizations were performed using a JEOL JEM2200FS microscope equipped with a Bruker energy-dispersive X-ray (EDX) detector, and with a Tecnai G2 20 TWIN instrument. The operation was at 200 kV and the electron probe size was set to be 0.2 and 0.7 nm for optimized imaging and spectroscopic analysis, respectively. TEM images were analyzed to determine the sizes of the particles with ImageJ[41] software.

SHG and Raman Experiments: To generate SHG, a laser operating at 850 nm with 150 fs pulses at 73 MHz repetition rate and a laser operating at 1064 nm with 6 ps pulses at 75 MHz repetition rate were used, respectively. The liquid samples were placed in microcontainers, the excitation light was focused onto the samples through a 10× microscope objective (NA 0.3), and the SHG light was detected in backscattering geometry by a liquid nitrogen cooled CCD detector. The signals were filtered with polarization-insensitive dichroic and bandpass filters with 20 nm full width. Hyper Raman spectra were excited with the 1064 nm laser, and Raman spectra were collected after excitation with a 785 nm continuous wave laser. The light was focused on the liquid samples through a 10× (NA 0.3) or 60× water immersion (NA 1.2) objective, and the scattered radiation was detected by a single-stage spectrograph with a CCD detector. The spectral resolution was ≈3–6 cm^{-1}, considering the full spectral range. All spectra were frequency calibrated using a spectrum of toluene/acetonitrile (1:1) mixture. SEHRS spectra were background corrected using an automatic background correction algorithm.[42] For all optical experiments, the integration times and excitation intensities are stated in the figure captions of the presented data.

Modification of the Nanoprobes for SHG and SERS Imaging Experiments in Cells: A previously reported protocol was adapted to displace the CTAB from the surface of the nanoparticles using lipids.[24] Liposomes were prepared by dissolving phosphatidylcholine in chloroform/methanol (1:1) mixture (10 g L^{-1}). Then, the solvent was removed under the stream of argon, and the dried lipids were rehydrated with PBS buffer. The mixture was freeze-thawed at least six times at the temperature of liquid nitrogen and at 37 °C. After freeze-thaw cycles, the lipids were sonicated and extruded through polycarbonate membrane (pore size 0.2 µm). The core–shell nanoparticles (50 µL) were mixed with the liposomes (100 µL), and sonicated for 20 min. After centrifugation and discarding the supernatant, the particles were redispersed in liposomes (200 µL) and sonicated for 20 min. This cycle was repeated three times. The particles were left over night in the lipid mixture at 4 °C, and finally centrifuged and redispersed in 1 mL water. For coating with pMBA, the core–shell nanoparticles (50 µL) were incubated with aqueous pMBA solution (950 µL, 5 × 10^{-5} M) over night. The excess pMBA was removed by centrifugation and the particles were redispersed in 1 mL water.

Experiments with Cultured Cells: Macrophages of cell line J774 (from DSMZ, Braunschweig, Germany) were cultured in DMEM supplemented with 10% FCS and 1% ZellShield in standard conditions (37 °C and 5% CO_2). For SHG and SERS experiments, the cells were grown as a monolayer on sterile cover slips (Thermo Fisher Scientific, Schwerte, Germany) in a six-well plate and incubated with 120 µL of lipid coated nanoparticles and 880 µL of cell culture medium for 3 h. Before the measurements, cells were thoroughly washed with PBS buffer, in which they were also kept while under the microscope. SERS and SHG maps were obtained by focusing the laser light with a 60× water immersion objective (NA 1.2) and raster scanning areas with a step size of 1 µm. Images of the signals were constructed using MatLab software.

Numerical and Analytical Simulations: Finite difference time domain (FDTD) numerical simulations were carried out with Lumerical FDTD Solutions 8.18. In these simulations, a plane wave polarized in the x direction and propagating in the −z direction excites a $BaTiO_3$ sphere (200, 255, or 300 nm in diameter or a 250 nm long rounded cuboid) and, for the coated case, the same structure surrounded by many uniformly distributed gold spheres of 17 nm diameter. The amount of gold nanospheres is chosen in a way that the total volume filling fraction of gold is ≈0.287 in all cases (e.g., corresponding to 600 gold spheres for the 300 nm $BaTiO_3$ sphere). All systems are located in water. The mesh used for the simulations was set finer in the region close to the sphere (or the cube), where the step is 5 nm for the simulations with bare $BaTiO_3$ particles and 0.5 nm for the simulations with Au@$BaTiO_3$ structures. The fields in the integrals for $BaTiO_3$ particles (Figure 8; Figure S15, Supporting Information, black lines) correspond to the values from individual mesh cells, but for Au@$BaTiO_3$ structures the fields in the integrals (Figure 8; Figure S15, Supporting Information, red lines) represent the averages over regions of 2.5 nm. This average

can lead to an underestimation of the contribution of the plasmonic hot spots to the SHG, but at the same time it helps to minimize the known problem with FDTD of obtaining artificially strong fields at regions very close to the interfaces. The study of the convergence is shown in Figure S12 in the Supporting Information. The frequency-dependent dielectric functions of barium titanate[43] and gold[44] were taken from the literature. For simplicity, any size correction to the gold permittivity is not considered.[45] The dielectric constant of the surrounding water was set to 1.7689.

The Mie analytical solution of the electromagnetic response[33] of the bare $BaTiO_3$ sphere in water allows to analyze the spectral peaks as the contributions of different multipoles of the dielectric sphere. The Mie extinction spectra were calculated using a 50-mode expansion (where each mode corresponds to an electric and a magnetic multipole). It is checked that these results do not differ from those obtained using a 15-mode expansion.

In the case of the $BaTiO_3$ sphere surrounded by gold nanospheres, a model that treats the gold coating as an effective shell is also employed.[21e] This shell has a thickness equal to the gold nanoparticles diameter (17 nm), and an effective permittivity that follows the Maxwell–Garnett effective medium theory formula

$$\varepsilon_{eff}(\omega) = \varepsilon_{H_2O} \frac{\varepsilon_{Au}(\omega)[1+2f] - \varepsilon_{H_2O}[2f-2]}{\varepsilon_{H_2O}[2+f] + \varepsilon_{Au}[1-f]} \tag{2}$$

where ω is the angular frequency, ε_{H_2O} is the permittivity of the surrounding water, ε_{Au} is the permittivity of the gold nanoparticles, and f is the filling fraction that represents the percentage of the volume that the 600 gold nanoparticles of 17 nm diameter occupy in the 17 nm thickness shell, $f = 0.287$ in our case. The resulting system of two concentric spheres is solved within Mie's framework.[35] All permittivity values used for the Mie theory are the same as for the FDTD simulations.

Supporting Information

Supporting Information is available from the Wiley Online Library or from the author.

Acknowledgements

Conflict of Interest

The authors declare no conflict of interest.

[1] a) J. W. Lichtman, J.-A. Conchello, *Nat. Methods* **2005**, *2*, 910; b) X. Michalet, A. N. Kapanidis, T. Laurence, F. Pinaud, S. Doose, M. Pflughoefft, S. Weiss, *Annu. Rev. Biophys. Biomol. Struct.* **2003**, *32*, 161.

[2] a) R. Zhang, Y. Zhang, Z. C. Dong, S. Jiang, C. Zhang, L. G. Chen, L. Zhang, Y. Liao, J. Aizpurua, Y. Luo, J. L. Yang, J. G. Hou, *Nature* **2013**, *498*, 82; b) S. Keren, C. Zavaleta, Z. Cheng, A. de la Zerda, O. Gheysens, S. S. Gambhir, *Proc. Natl. Acad. Sci. USA* **2008**, *105*, 5844.

[3] a) W. Denk, J. Strickler, W. Webb, *Science* **1990**, *248*, 73; b) Y. Qiang, P. Artoni, K. J. Seo, S. Culaclii, V. Hogan, X. Zhao, Y. Zhong, X. Han, P.-M. Wang, Y.-K. Lo, Y. Li, H. A. Patel, Y. Huang, A. Sambangi, J. S. V. Chu, W. Liu, M. Fagiolini, H. Fang, *Sci. Adv.* **2018**, *4*, eaat0626.

[4] a) I. Freund, M. Deutsch, A. Sprecher, *Biophys. J.* **1986**, *50*, 693; b) B. Wen, K. R. Campbell, K. Tilbury, O. Nadiarnykh, M. A. Brewer, M. Patankar, V. Singh, K. W. Eliceiri, P. J. Campagnola, *Sci. Rep.* **2016**, *6*, 35734; c) Z. Heiner, I. Zeise, R. Elbaum, J. Kneipp, *J. Biophotonics* **2018**, *11*, e201700164.

[5] a) C. W. Freudiger, W. Min, B. G. Saar, S. Lu, G. R. Holtom, C. He, J. C. Tsai, J. X. Kang, X. S. Xie, *Science* **2008**, *322*, 1857; b) M. Ji, M. Arbel, L. Zhang, C. W. Freudiger, S. S. Hou, D. Lin, X. Yang, B. J. Bacskai, X. S. Xie, *Sci. Adv.* **2018**, *4*, eaat7715.

[6] a) A. Volkmer, J.-X. Cheng, X. Sunney Xie, *Phys. Rev. Lett.* **2001**, *87*, 023901; b) H. Wang, S. Osseiran, V. Igras, A. J. Nichols, E. M. Roider, J. Pruessner, H. Tsao, D. E. Fisher, C. L. Evans, *Sci. Rep.* **2016**, *6*, 37986.

[7] a) R. Shimada, H. Kano, H.-o. Hamaguchi, *Opt. Lett.* **2006**, *31*, 320; b) J. Kneipp, H. Kneipp, K. Kneipp, *Proc. Natl. Acad. Sci. USA* **2006**, *103*, 17149; c) M. Guhlke, Z. Heiner, J. Kneipp, *Phys. Chem. Chem. Phys.* **2016**, *18*, 14228.

[8] a) W. R. Zipfel, R. M. Williams, W. W. Webb, *Nat. Biotechnol.* **2003**, *21*, 1369; b) F. Helmchen, W. Denk, *Nat. Methods* **2005**, *2*, 932.

[9] F. Madzharova, Z. Heiner, J. Kneipp, *Chem. Soc. Rev.* **2017**, *46*, 3980.

[10] a) T. Terai, T. Nagano, *Pflügers Arch. – Eur. J. Physiol.* **2013**, *465*, 347; b) M. Pawlicki, H. A. Collins, R. G. Denning, H. L. Anderson, *Angew. Chem., Int. Ed.* **2009**, *48*, 3244.

[11] I. L. Medintz, H. T. Uyeda, E. R. Goldman, H. Mattoussi, *Nat. Mater.* **2005**, *4*, 435.

[12] a) P. Pantazis, J. Maloney, D. Wu, S. E. Fraser, *Proc. Natl. Acad. Sci. USA* **2010**, *107*, 14535; b) D. Staedler, T. Magouroux, R. Hadji, C. Joulaud, J. Extermann, S. Schwung, S. Passemard, C. Kasparian, G. Clarke, M. Gerrmann, R. Le Dantec, Y. Mugnier, D. Rytz, D. Ciepielewski, C. Galez, S. Gerber-Lemaire, L. Juillerat-Jeanneret, L. Bonacina, J.-P. Wolf, *ACS Nano* **2012**, *6*, 2542.

[13] a) J. Kneipp, *ACS Nano* **2017**, *11*, 1136; b) F. Madzharova, Z. Heiner, J. Simke, S. Selve, J. Kneipp, *J. Phys. Chem. C* **2018**, *122*, 2931.

[14] T. Meyer, M. Schmitt, B. Dietzek, J. Popp, *J. Biophotonics* **2013**, *6*, 887.

[15] a) E. De Meulenaere, W.-Q. Chen, S. Van Cleuvenbergen, M.-L. Zheng, S. Psilodimitrakopoulos, R. Paesen, J.-M. Taymans, M. Ameloot, J. Vanderleyden, P. Loza-Alvarez, X.-M. Duan,

K. Clays, *Chem. Sci.* **2012**, *3*, 984; b) X. Jin, H. Li, S. Wang, N. Kong, H. Xu, Q. Fu, H. Gu, J. Ye, *Nanoscale* **2014**, *6*, 14360; c) T. Nagy-Simon, A.-S. Tatar, A.-M. Craciun, A. Vulpoi, M.-A. Jurj, A. Florea, C. Tomuleasa, I. Berindan-Neagoe, S. Astilean, S. Boca, *ACS Appl. Mater. Interfaces* **2017**, *9*, 21155; d) Z. Hu, G. D. Pantoş, N. Kuganathan, R. L. Arrowsmith, R. M. J. Jacobs, G. Kociok-Köhn, J. O'Byrne, K. Jurkschat, P. Burgos, R. M. Tyrrell, S. W. Botchway, J. K. M. Sanders, S. I. Pascu, *Adv. Funct. Mater.* **2012**, *22*, 503.

[16] a) J. Ćulić-Viskota, W. P. Dempsey, S. E. Fraser, P. Pantazis, *Nat. Protoc.* **2012**, *7*, 1618; b) W. P. Dempsey, S. E. Fraser, P. Pantazis, *BioEssays* **2012**, *34*, 351; c) G. G. Genchi, A. Marino, A. Rocca, V. Mattoli, G. Ciofani, *Nanotechnology* **2016**, *27*, 232001; d) N. Sugiyama, A. Y. Sonay, R. Tussiwand, B. E. Cohen, P. Pantazis, *Small* **2018**, *14*, 1703386.

[17] S.-J. Chang, W.-S. Liao, C.-J. Ciou, J.-T. Lee, C.-C. Li, *J. Colloid Interface Sci.* **2009**, *329*, 300.

[18] a) E. FarrokhTakin, G. Ciofani, G. L. Puleo, G. de Vito, C. Filippeschi, B. Mazzolai, V. Piazza, V. Mattoli, *Int. J. Nanomed.* **2013**, *8*, 2319; b) D.-H. Yoon, B. I. Lee, P. Badheka, X. Wang, *J. Mater. Sci.: Mater. Electron.* **2003**, *14*, 165.

[19] a) S. J. Oldenburg, S. L. Westcott, R. D. Averitt, N. J. Halas, *J. Chem. Phys.* **1999**, *111*, 4729; b) Y. Pu, R. Grange, C.-L. Hsieh, D. Psaltis, *Phys. Rev. Lett.* **2010**, *104*, 207402.

[20] L. Scarabelli, A. Sánchez-Iglesias, J. Pérez-Juste, L. M. Liz-Marzán, *J. Phys. Chem. Lett.* **2015**, *6*, 4270.

[21] a) F. Timpu, N. R. Hendricks, M. Petrov, S. Ni, C. Renaut, H. Wolf, L. Isa, Y. Kivshar, R. Grange, *Nano Lett.* **2017**, *17*, 5381; b) S. Mühlig, A. Cunningham, S. Scheeler, C. Pacholski, T. Bürgi, C. Rockstuhl, F. Lederer, *ACS Nano* **2011**, *5*, 6586; c) L. Jiang, Z. Wu, D. Wu, W. Yang, R. Jin, *Nanotechnology* **2007**, *18*, 185603; d) C. R. Simovski, S. A. Tretyakov, *Phys. Rev. B* **2009**, *79*, 045111; e) S. Mühlig, M. Farhat, C. Rockstuhl, F. Lederer, *Phys. Rev. B* **2011**, *83*, 195116.

[22] H. Kang, J.-K. Yang, M. S. Noh, A. Jo, S. Jeong, M. Lee, S. Lee, H. Chang, H. Lee, S.-J. Jeon, H.-I. Kim, M.-H. Cho, H.-Y. Lee, J.-H. Kim, D. H. Jeong, Y.-S. Lee, *J. Mater. Chem. B* **2014**, *2*, 4415.

[23] R. Esteban, R. W. Taylor, J. J. Baumberg, J. Aizpurua, *Langmuir* **2012**, *28*, 8881.

[24] J. R. Matthews, C. M. Payne, J. H. Hafner, *Langmuir* **2015**, *31*, 9893.

[25] a) A. L. Dendramis, E. W. Schwinn, R. P. Sperline, *Surf. Sci.* **1983**, *134*, 675. b) Spectral Database for Organic Compounds, https://sdbs.db.aist.go.jp/sdbs/cgibin/landingpage?sdbsno=2360 (accessed: August 2019). c) J. E. Stewart, *J. Chem. Phys.* **1959**, *30*, 1259. d) F. S. Parker, *Applications of Infrared, Raman and Resonance Raman Spectroscopy in Biochemistry*, Plenum Press, New York **1984**, p. 29.

[26] a) D. Drescher, P. Guttmann, T. Büchner, S. Werner, G. Laube, A. Hornemann, B. Tarek, G. Schneider, J. Kneipp, *Nanoscale* **2013**, *5*, 9193; b) D. Drescher, I. Zeise, H. Traub, P. Guttmann, S. Seifert, T. Büchner, N. Jakubowski, G. Schneider, J. Kneipp, *Adv. Funct. Mater.* **2014**, *24*, 3765.

[27] J. Kneipp, H. Kneipp, M. McLaughlin, D. Brown, K. Kneipp, *Nano Lett.* **2006**, *6*, 2225.

[28] V. Živanović, Z. Kochovski, C. Arenz, Y. Lu, J. Kneipp, *J. Phys. Chem. Lett.* **2018**, *9*, 6767.

[29] a) Z. Movasaghi, S. Rehman, I. U. Rehman, *Appl. Spectrosc. Rev.* **2007**, *42*, 493; b) F. Madzharova, Z. Heiner, J. Kneipp, *J. Phys. Chem. C* **2017**, *121*, 1235.

[30] a) A. V. Baranov, Y. S. Bobovich, *JETP Lett.* **1982**, *36*, 339; b) W. Leng, A. M. Kelley, *J. Am. Chem. Soc.* **2006**, *128*, 3492; c) T. Itoh, Y. Ozaki, H. Yoshikawa, T. Ihama, H. Masuhara, *Appl. Phys. Lett.* **2006**, *88*, 084102.

[31] a) M. Gühlke, Z. Heiner, J. Kneipp, *Phys. Chem. Chem. Phys.* **2015**, *17*, 26093; b) Z. Heiner, M. Gühlke, V. Živanović, F. Madzharova, J. Kneipp, *Nanoscale* **2017**, *9*, 8024.

[32] A. Michota, J. Bukowska, *J. Raman Spectrosc.* **2003**, *34*, 21.

[33] C. F. Bohren, D. R. Huffman, *Absorption and Scattering of Light by Small Particles*, Wiley, New York **1998**.

[34] a) P. Albella, M. A. Poyli, M. K. Schmidt, S. A. Maier, F. Moreno, J. J. Sáenz, J. Aizpurua, *J. Phys. Chem. C* **2013**, *117*, 13573; b) A. García-Etxarri, R. Gómez-Medina, L. S. Froufe-Pérez, C. López, L. Chantada, F. Scheffold, J. Aizpurua, M. Nieto-Vesperinas, J. J. Sáenz, *Opt. Express* **2011**, *19*, 4815; c) F. Timpu, A. Sergeyev, N. R. Hendricks, R. Grange, *ACS Photonics* **2017**, *4*, 76; d) M. Caldarola, P. Albella, E. Cortes, M. Rahmani, T. Roschuk, G. Grinblat, R. F. Oulton, A. V. Bragas, S. A. Maier, *Nat. Commun.* **2015**, *6*, 7915; e) T. G. Habteyes, I. Staude, K. E. Chong, J. Dominguez, M. Decker, A. Miroshnichenko, Y. Kivshar, I. Brener, *ACS Photonics* **2014**, *1*, 794.

[35] A. L. Aden, M. Kerker, *J. Appl. Phys.* **1951**, *22*, 1242.

[36] a) C. Ma, J. Yan, Y. Wei, P. Liu, G. Yang, *J. Mater. Chem. C* **2017**, *5*, 4810; b) S. V. Makarov, M. I. Petrov, U. Zywietz, V. Milichko, D. Zuev, N. Lopanitsyna, A. Kuksin, I. Mukhin, G. Zograf, E. Ubyivovk, D. A. Smirnova, S. Starikov, B. N. Chichkov, Y. S. Kivshar, *Nano Lett.* **2017**, *17*, 3047.

[37] a) R. Carminati, M. Nieto-Vesperinas, J.-J. Greffet, *J. Opt. Soc. Am. A* **1998**, *15*, 706; b) P. Bharadwaj, B. Deutsch, L. Novotny, *Adv. Opt. Photonics* **2009**, *1*, 438; c) R. Esteban, M. Laroche, J.-J. Greffet, *J. Appl. Phys.* **2009**, *105*, 033107.

[38] a) E. V. Makeev, S. E. Skipetrov, *Opt. Commun.* **2003**, *224*, 139; b) M. Baudrier-Raybaut, R. Haïdar, P. Kupecek, P. Lemasson, E. Rosencher, *Nature* **2004**, *432*, 374; c) S. Brasselet, V. Le Floc'h, F. Treussart, J.-F. Roch, J. Zyss, E. Botzung-Appert, A. Ibanez, *Phys. Rev. Lett.* **2004**, *92*, 207401.

[39] a) J. Chen, P. Albella, Z. Pirzadeh, P. Alonso-González, F. Huth, S. Bonetti, V. Bonanni, J. Åkerman, J. Nogués, P. Vavassori, A. Dmitriev, J. Aizpurua, R. Hillenbrand, *Small* **2011**, *7*, 2341; b) J. Zuloaga, P. Nordlander, *Nano Lett.* **2011**, *11*, 1280.

[40] D. G. Duff, A. Baiker, P. P. Edwards, *Langmuir* **1993**, *9*, 2301.

[41] C. A. Schneider, W. S. Rasband, K. W. Eliceiri, *Nat. Methods* **2012**, *9*, 671.

[42] Z.-M. Zhang, S. Chen, Y.-Z. Liang, Z.-X. Liu, Q.-M. Zhang, L.-X. Ding, F. Ye, H. Zhou, *J. Raman Spectrosc.* **2010**, *41*, 659.

[43] C. Wong, Y. Y. Teng, J. Ashok, P. L. H. Varaprasad, in *Handbook of Optical Constants of Solids* (Ed: E. D. Palik), Academic Press, Burlington, VT **1997**, p. 789.

[44] P. B. Johnson, R. W. Christy, *Phys. Rev. B* **1972**, *6*, 4370.

[45] S. Berciaud, L. Cognet, P. Tamarat, B. Lounis, *Nano Lett.* **2005**, *5*, 515.